Can Existing Theory Predict the Response of Tropical Cyclone Intensity to Idealized Landfall?

JIE CHEN[a] AND DANIEL R. CHAVAS[a]

[a] *Department of Earth, Atmospheric, and Planetary Sciences, Purdue University, West Lafayette, Indiana*

(Manuscript received 8 February 2021, in final form 11 June 2021)

ABSTRACT: Tropical cyclones cause significant inland hazards, including wind damage and freshwater flooding, which depend strongly on how storm intensity evolves after landfall. Existing theoretical predictions for storm intensification and equilibrium storm intensity have been tested over the open ocean but have not yet been applied to storms after landfall. Recent work examined the transient response of the tropical cyclone low-level wind field to instantaneous surface roughening or drying in idealized axisymmetric *f*-plane simulations. Here, experiments testing combined surface roughening and drying with varying magnitudes of each are used to test theoretical predictions for the intensity response. The transient response to combined surface forcings can be reproduced by the product of their individual responses, in line with traditional potential intensity theory. Existing intensification theory is generalized to weakening and found capable of reproducing the time-dependent inland intensity decay. The initial (0–10 min) rapid decay of near-surface wind caused by surface roughening is not captured by existing theory but can be reproduced by a simple frictional spindown model, where the decay rate is a function of surface drag coefficient. Finally, the theory is shown to compare well with the prevailing empirical decay model for real-world storms. Overall, results indicate the potential for existing theory to predict how tropical cyclone intensity evolves after landfall.

KEYWORDS: Hurricanes; Tropical cyclones; Idealized models; Land surface; Risk assessment

1. Introduction

Landfalling tropical cyclones (TCs) bring tremendous damage to both coastal and inland regions (Rappaport 2000, 2014; Villarini et al. 2014). These damages may change in the future should TCs move and/or decay more slowly in a warming climate (Kossin 2018, 2019; Li and Chakraborty 2020). Therefore, a credible estimation of TC intensity decay after landfall is essential for hazard prediction. Having a physically based theoretical solution for the storm intensity response to landfall could help improve risk assessment, both in real-time impending landfall events and in climatological studies (Jing and Lin 2020; Xi et al. 2020). However, the underlying physics governing this postlandfall response are not well understood, and no such predictive theory currently exists.

Past research has examined TC intensity at and after landfall via numerical simulations and statistical models. Idealized simulations have been applied to understand the intensity decay (Tuleya and Kurihara 1978). More recently, numerical models have been used to simulate real-world landfalls that can capture more complex details of the storm evolution, yet such models still have a limited capacity to predict postlandfall intensity due to the difficulty of capturing the physics over complex terrain (e.g., Davis et al. 2008; Jin et al. 2010). These limitations are not necessarily improved by increasing model resolution or assimilating observational data (Liu et al. 2017). Moreover, site-specific case studies are not readily generalized to a more fundamental understanding of the storm response to landfall over a wide range of land surfaces. An alternative approach is the use of empirical models or probabilistic models to predict storm inland intensity decay, which may incorporate both storm and environmental parameters (Kaplan and DeMaria 1995, 2001; Vickery and Twisdale 1995; Vickery 2005; DeMaria et al. 2006; Bhowmik et al. 2005). Empirical models have been incorporated into the Statistical Hurricane Intensity Prediction Scheme for the Atlantic and eastern Pacific Oceans (DeMaria and Kaplan 1994; DeMaria et al. 2005) and Statistical Typhoon Intensity Prediction Scheme for the western North Pacific (Knaff et al. 2005), and have been tested for landfalling hurricanes along the South China Coast (Wong et al. 2008). Statistical models have also been incorporated into TC risk assessment models in the context of climate change (Vickery et al. 2000; Emanuel et al. 2006; Jing and Lin 2020). However, current statistical models do not incorporate the physics of TC intensity decay over land, and their accuracy is limited by the data collected to train the model. Thus, empirical models offer limited fundamental understanding of the inland decay of TC intensity, particularly under a changing climate.

Physically based theoretical models are formulated for TCs over the ocean. Quasi-steady-state theories for the tropical cyclone date back to Lilly and Emanuel (1985, unpublished manuscript), Shutts (1981), Emanuel (1986, hereafter E86). More recently, Emanuel (2012, hereafter E12) provides a new solution for TC intensification over the ocean that was derived from the self-stratified outflow theory of Emanuel and Rotunno (2011). However, due to the complexities in the transition from ocean to land, research has yet to develop a theory for postlandfall decay that accounts for the basic physics of the response of a tropical cyclone to landfall. Meanwhile, the potential for existing theoretical models for storms over the

Supplemental information related to this paper is available at the Journals Online website: https://doi.org/10.1175/JAS-D-21-0037.s1.

Corresponding author: Jie Chen, chenjie@princeton.edu

DOI: 10.1175/JAS-D-21-0037.1

ocean to be applied after landfall has yet to be explored. Therefore, testing existing theories against idealized landfalls is a natural step to understand how well-known physics can explain the response of TC intensity after landfall. This is the focus of our work.

Chen and Chavas (2020, hereafter CC20) idealized the landfall as a transient response of a mature axisymmetric TC to instantaneous surface forcing: surface roughening or drying, each over a range of magnitudes. Idealized modeling simplifies the complicated landfall processes to isolate and understand the most fundamental physics underlying the inland evolution. They tested the response to each forcing individually and showed that each ultimately causes the storm to weaken but via different mechanistic pathways. They further showed that the final equilibrium intensity in response to each forcing can be predicted by E86 potential intensity theory. A logical next step is to test whether the transient intensity response can be predicted by existing theory and, further, whether results can be generalized to any combination of surface drying and roughening applied simultaneously. Both outcomes would be more directly relevant to a wide range of inland surfaces felt by storms in real-world landfalls.

Therefore, in this work, both steady-state intensity theory (E86) and time-dependent intensity change theory (E12) are tested against sets of simulations where surface roughness and wetness are individually or simultaneously modified instantaneously beneath a mature axisymmetric tropical cyclone. We seek to answer the following research questions:

1) Can traditional potential intensity theory predict the equilibrium intensity response to simultaneous surface drying and roughening?
2) Can the transient intensity response to simultaneous drying and roughening be predicted from the responses to each forcing individually?
3) Can existing intensification theory predict the transient intensity weakening response to surface drying and/or roughening?
4) Do the theories work for the intensity both near the surface and near the top of the boundary layer (above-BL)?

This paper is structured as follows. Section 2 reviews the relevant theories and demonstrates how they may be applied to predict the intensity response to surface forcings. Section 3 describes our idealized simulation experiments that are used to test the theory. Section 4 presents our results addressing the research questions. Section 5 summarizes key results, limitations, and avenues for future work.

2. Theory

This work examines two existing theories that predict the equilibrium intensity (E86) and the time-dependent intensity change (E12) of a tropical cyclone. The original motivation of such theories is for storms over the ocean. CC20 found that the equilibrium response of a mature TC to instantaneous surface roughening or drying followed the response predicted by E86 theory closely. This work expands on CC20 by testing both the E86 and E12 theory and generalizes the experiments to simultaneous surface roughening and drying. This section reviews each theoretical prediction and demonstrates how they can be formulated to apply to idealized landfall experiments.

a. *Equilibrium intensity prediction: E86*

Potential intensity is a theoretical upper-bound for the tropical cyclone intensity in a given thermodynamic environment. This theory is formulated by idealizing a mature tropical cyclone as a Carnot heat engine, where enthalpy fluxes from the ocean surface are used to maintain the circulation against surface frictional dissipation. The formulation of potential intensity V_p applied in this work includes the effect of dissipative heating, which results in the tropopause temperature replacing the surface temperature in the denominator of the Carnot efficiency factor (Bister and Emanuel 1998) compared to Emanuel (1986),

$$V_p = \sqrt{\frac{C_k}{C_d}\eta(\Delta k)}, \tag{1}$$

with Carnot efficiency given by

$$\eta = \frac{T_{\mathrm{ST}} - T_{\mathrm{tpp}}}{T_{\mathrm{tpp}}} \tag{2}$$

and

$$\Delta k = C_p \Delta T + \varepsilon L_v \Delta q = C_p (T_{\mathrm{ST}} - T_a) + \varepsilon L_v \left[q^*_{(T_{\mathrm{ST}})} - q_{a(T_a)} \right], \tag{3}$$

where C_k and C_d are bulk exchange coefficients for surface enthalpy and momentum, respectively; Δk is the difference between the environmental saturation enthalpy of the ocean surface and the enthalpy of the overlying near-surface air, where we define ΔT and Δq from the environment (averaged over r = 1500–2500 km in our simulations below); T_{ST} is the surface temperature; T_a is the temperature of air overlying the surface; T_{tpp} is the tropopause temperature; L_v is the latent heat of vaporization; C_p is the specific heat capacity of air; $q^*_{(T_{\mathrm{ST}})}$ is the saturation mixing ratio of the ocean surface at the local surface pressure; $q_{a(T_a)}$ is the mixing ratio of air overlying the ocean surface; and ε is surface evaporative fraction, which is set to 1 to represent an ocean-like surface in this work. Physically, Eq. (1) is derived from a simple energy balance at the surface: surface heat fluxes are the energy source that can be used to generate kinetic energy while surface friction is the energy sink that removes kinetic energy. The potential intensity serves as a general prediction for the equilibrium intensity that can be calculated strictly from environmental quantities via Eq. (1).

Hence, for a storm that moves over rougher (higher C_d) and drier (smaller ε) surface, Eq. (1) predicts a weaker equilibrium intensity compared to the ocean surface. We define the response of V_p to any given surface forcing, surface roughening or drying, as the ratio of its postforcing value to its initial preforcing value. As was done in CC20, Eq. (1) may be used to define the predicted V_p response to surface roughening, $\tilde{V}_{p,C_d}$, as a ratio of the final value to the initial preforcing value:

$$\tilde{V}_{p,C_d} = \frac{V_{p,C_d}}{V_{p,\mathrm{CTRL}}} = \frac{\sqrt{\frac{C_k}{C_{d,\mathrm{exp}}}\eta(C_p\Delta T + \varepsilon L_v \Delta q)}}{\sqrt{\frac{C_k}{C_{d,\mathrm{CTRL}}}\eta(C_p\Delta T + \varepsilon L_v \Delta q)}} = \sqrt{\frac{C_{d,\mathrm{CTRL}}}{C_{d,\mathrm{exp}}}}, \tag{4}$$

where $V_{p,\mathrm{CTRL}}$ is the potential intensity of a Control prelandfall TC (defined in section 3) where $C_{d,\mathrm{CTRL}}$ is the initial Control value of surface drag coefficient; $C_{d,\mathrm{EXP}}$ is the enhanced drag coefficient applied in the roughening experiment. The quantity Δk defined and calculated from the environment in RCE is not very sensitive to C_d and so may be taken as a constant between $V_{p,\mathrm{CTRL}}$ and V_{p,C_d}, and hence it cancels out in Eq. (4). Similarly, surface drying is given by

$$\tilde{V}_{p,\varepsilon} = \frac{V_{p,\varepsilon}}{V_{p,\mathrm{CTRL}}} = \frac{\sqrt{\frac{C_k}{C_d}\eta(C_p\Delta T + \varepsilon_{\mathrm{exp}} L_v \Delta q)}}{\sqrt{\frac{C_k}{C_d}\eta(C_p\Delta T + \varepsilon_{\mathrm{CTRL}} L_v \Delta q)}} = \sqrt{\frac{C_p\Delta T + \varepsilon_{\mathrm{exp}} L_v \Delta q}{\Delta k_{\mathrm{CTRL}}}}, \tag{5}$$

where $\varepsilon_{\mathrm{CTRL}}$ is the default evaporative fraction over an oceanic surface while $\varepsilon_{\mathrm{EXP}}$ is the reduced ε indicating a drier surface. As discussed in CC20, using normalized responses of V_p can generalize the results to any mature storm intensity and also minimize sensitivities associated with the precise definition of V_p. CC20 demonstrated that the final equilibrium intensity response in idealized simulations closely follows this prediction.

Here we expand this approach to simultaneous surface drying and roughening. In this scenario, the energy source is reduced (drying) and the energy sink is enhanced (roughening). This results in an even weaker potential intensity $V_{p,C_d\varepsilon}$, i.e., a stronger response of the equilibrium intensity, than the response to either forcing individually. This response is given by

$$\tilde{V}_{p,C_d\varepsilon} = \frac{\sqrt{\frac{C_k}{C_{d,\mathrm{exp}}}\eta(C_p\Delta T + \varepsilon_{\mathrm{exp}} L_v \Delta q)}}{\sqrt{\frac{C_k}{C_{d,\mathrm{CTRL}}}\eta(C_p\Delta T + \varepsilon_{\mathrm{CTRL}} L_v \Delta q)}} = \sqrt{\frac{C_{d,\mathrm{CTRL}}}{C_{d,\mathrm{exp}}}}\sqrt{\frac{C_p\Delta T + \varepsilon_{\mathrm{exp}} L_v \Delta q}{\Delta k_{\mathrm{CTRL}}}} = \tilde{V}_{p,C_d}\tilde{V}_{p,\varepsilon}. \tag{6}$$

Mathematically, Eq. (6) indicates that the equilibrium intensity response to simultaneous forcing, $\tilde{V}_{p,C_d\varepsilon}$, is simply the product of the individual equilibrium responses $\tilde{V}_{p,C_d}$ and $\tilde{V}_{p,\varepsilon}$.

Inspired by Eq. (6), we hypothesize that the complete time-dependent response of storm intensity $\tilde{v}_{m,C_d\varepsilon}(\tau)$ to simultaneous surface roughening and drying may be predicted by the product of the individual transient responses, i.e.,

$$\tilde{v}_{m,C_d\varepsilon}(\tau) \approx \tilde{v}^*(\tau) = \tilde{v}_{m,C_d}(\tau)\tilde{v}_{m,\varepsilon}(\tau), \tag{7}$$

where τ is time since the instantaneous change in surface forcing. The relationship described in Eq. (6) and the hypothesis made in Eq. (7) are tested below. If true, this outcome would have significant practical benefits for understanding the intensity response to a wide range of surface properties as is found in nature. Notably, there is an alternative definition of potential intensity that accounts for the role of gradient wind imbalance and its impact on vertical velocity within the eyewall and predicts a secondary dependence on the ratio C_k/C_d (Bryan 2012). However, this more complex version depends on time-dependent knowledge of the inner-core storm structure. Thus, here we elect to focus on the simpler Eq. (6), a prediction that depends only on external environmental parameters and provides a straightforward avenue to deconstruct and understand the responses to combined surface forcing via Eqs. (6) and (7).

b. *Transient intensity prediction: E12*

E12 presents a theory for the time-dependent intensification of a TC. This theory is derived from Emanuel and Rotunno (2011), where the outflow self-stratification determines the radial distribution of the low-level entropy and angular momentum at the top of a slab boundary layer. The outflow turbulence processes that underlie this theory have been found in observations and models (Molinari and Duran 2014; Duran and Molinari 2018; Tao et al. 2019), though the extent to which turbulence sets the outflow stratification is debated (Montgomery et al. 2019; Peng et al. 2018, 2019). The E12 intensification solution compares well against simulations after the initial spinup period in an axisymmetric model varying C_k but holding C_d constant, while the theoretical intensification rate is sensitive to the C_d when keep C_k constant (Emanuel 2018). Peng et al. (2018) suggests that this sensitivity to C_d results from the neglected effects of nongradient wind in Emanuel's study. The original E12 equation is given by

$$v_m(\tau) = v_f \tanh\left(\frac{C_k v_f}{2h}\tau\right), \tag{8}$$

with initial condition $v_m = 0$ at $\tau = 0$, v_f is the final steady-state maximum wind speed that estimated by the potential intensity [Eq. (19) of Emanuel (2012)]; h is a constant boundary layer depth scale within the eyewall, which is set as 5 km in Emanuel (2012) and is discussed at the end of this section.

Ramsay et al. (2020) generalized Eq. (8) to predict the intensification from a nonzero initial intensity. Here we further generalize Eq. (8) (see the appendix) to represent the decay from an initial intensity $v_{m,0}$ to a weaker equilibrium intensity v_f as

$$v_{m,\mathrm{th}}(\tau) = v_f \coth\left[\frac{C_k v_f}{2h}\tau + \tanh^{-1}\left(\frac{v_f}{v_{m,0}}\right)\right]. \tag{9}$$

This can be written in a form normalized by the initial intensity, given by

$$\tilde{v}_{m,\mathrm{th}}(\tau) = \frac{v_{m,\mathrm{th}}(\tau)}{v_{m,0}} = \tilde{v}_f \coth\left[\frac{C_k v_f}{2h}\tau + \tanh^{-1}(\tilde{v}_f)\right], \tag{10}$$

where $\tilde{v}_f = v_f/v_{m,0}$. One may apply $\tilde{V}_p$ calculated from Eqs. (4)–(6) to approximate $\tilde{v}_f$. In this paper, we use the subscript "th" to denote the intensity predicted by theory.

According to Eq. (10), the intrinsic time scale of intensity decay from the initial condition, $2h/(C_k v_f)$, is determined by the boundary layer depth scale h and the steady-state final intensity v_f when taking C_k as constant. First, for v_f, effects from changes in the external environment, e.g., surface properties including ε and C_d, are captured by v_f. Thus, higher C_d or/and smaller ε produces a smaller $\tilde{v}_f$ in Eq. (10) as well as a higher decay rate for fixed h. Examples of the theoretical prediction of Eq. (10) are presented in Fig. 1a for a range of v_f, using the value of h (5 km) applied in Emanuel (2012) and an initial intensity of 100 m s^{-1}. For the special case where $v_f = 0$, the solution, derived directly from (A1), simplifies to

$$\tilde{v}_{m,\mathrm{th}}(\tau) = \left(\frac{C_k v_{m,0}}{2h}\tau + 1\right)^{-1}. \tag{11}$$

For this case, the transient intensity response from a given $v_{m,0}$ depends only on the boundary layer depth scale h. Equation (11) is the continuous limit of Eq. (10) as $v_f \to 0$ and is not singular. Second, for h, a smaller h produces a faster decay. Figure 1b presents examples varying h over a wide range of values, with $v_{m,0} = 100$ m s^{-1} and $v_f = 0$. Note that setting $v_f = 0$ produces a solution that does not actually reach zero intensity in finite time (for any h), but rather approaches zero only as $\tau \to \infty$; for realistic time scales, the solution still predicts a normalized intensity appreciably greater than zero (≈15% of the initial value after 5 days in Fig. 1a).

The precise definition of h in E12 theory and its relation to the true boundary layer height H is uncertain both theoretically and practically. First and foremost, the TC boundary layer height H is poorly understood even for storms over the ocean where H is approximated by its dynamical or thermodynamical characteristics (Kepert 2001; Emanuel 1997; Bryan and Rotunno 2009; Zhang et al. 2011; Seidel et al. 2010). Unfortunately, these estimates of boundary layer heights can vary substantially from one another (Zhang et al. 2011). Moreover, in the E12 theory, it is the boundary layer depth specifically within the deeply convecting eyewall that is relevant, where air rapidly rising out of the boundary layer and effectively blurs the distinction between the boundary layer and free troposphere (Marks et al. 2008; Kepert 2010; Smith and Montgomery 2010). Perhaps for this reason E12 found a value corresponding to an approximate half-depth of the troposphere (5 km) to perform best. Finally, little is known about the TC boundary layer height during the landfall transition, and there may be multiple distinct boundary layers that evolve in time (Alford et al. 2020). Thus, when evaluating E12 theory, we simply test a range of values for h and examine the extent to which variations in the best-fit values of h across experiments align with variations in estimates of the boundary layer height H.

3. Methodology

Idealized numerical simulation experiments of landfall are used to test the theoretical predictions discussed in the previous section.

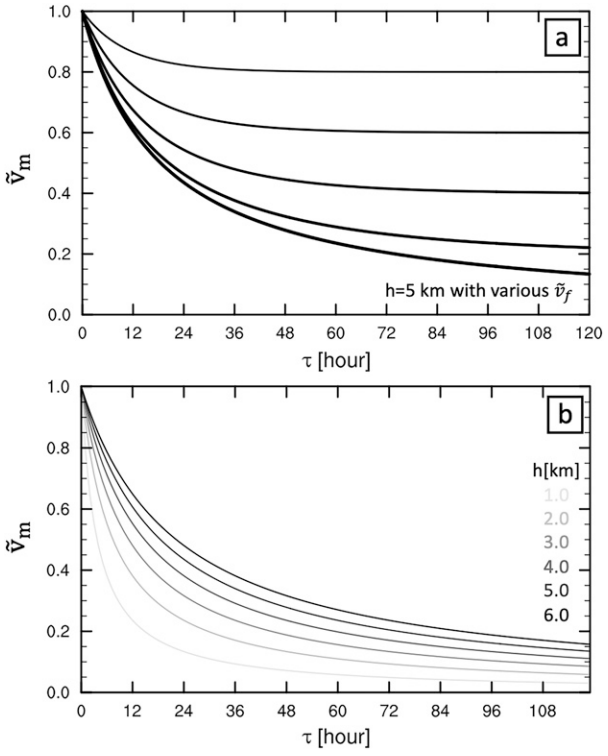

FIG. 1. Normalized intensity decay predicted by E12 theory with $v_{m,0} = 100$ m s^{-1}: (a) varying $\tilde{v}_f$ with $h = 5$ km, for $v_f = 80\%$, 60%, 40%, 20%, and 0% of initial intensity [Eq. (10)]; and (b) varying h with $\tilde{v}_f = 0$ [Eq. (11)]. Note that for $\tilde{v}_f = 0$, intensity reaches zero only as $\tau \to \infty$.

a. Simulation setup

The pronounced spatiotemporal heterogeneity in surface properties from storm to storm in real-world landfalls requires sophisticated land surface and boundary layer parameterizations (Cosby et al. 1984; Stull 1988; Davis et al. 2008; Nolan et al. 2009; Jin et al. 2010). However, experiments in axisymmetric geometry with a uniform environment and uniform boundary forcing can reveal the fundamental responses of a mature TC to individual surface roughening or drying, as introduced in CC20. Thus, this work extends the experimental design of CC20 for individual forcings to simulations where the surface is simultaneously dried and roughened with varying magnitudes of each.

All experiments are performed using the Bryan Cloud Model (CM1v19.8) (Bryan and Fritsch 2002) in axisymmetric geometry with same setup as Chen and Chavas (2020). CM1 solves the fully compressible equation of motion in height coordinates on an f plane on a fully staggered Arakawa C-type grid. Model parameters are summarized in Table 1, with a horizontal domain $L = 3000$ km and 3-km radial grid spacing. A stretched grid is used vertically with a constant grid spacing of 100 m below $z = 3$ km, smoothly stretching to 500 m at $z = 3$ km, and then constant grid spacing of 500 m from $z = 12$ to 25 km. In axisymmetric geometry, turbulent eddies cannot be resolved directly and thus their effects are parameterized

TABLE 1. Parameter values of the CTRL simulation.

Model	Name	Value	Environment	Name	Value
l_h	Horizontal mixing length	750 m	T_{ST}	Surface temperature	300 K
l_{inf}	Asymptotic vertical mixing length	100 m	T_{tpp}	Tropopause temperature	200 K
C_k, C_d	Exchange coefficients of enthalpy and momentum	0.0015	Q_{cool}	Radiative cooling rate (potential temperature)	1 K day^{-1}
H_{domain}	Height of model top	25 km	f	Coriolis parameter	5×10^{-5} s^{-1}
L_{domain}	Radius of model outer wall	3000 km			
Δx	Horizontal grid spacing	3 km			
Δz	H = 0–3 km: fixed vertical grid spacing	0.1 km			
	H = 3–12 km: stretching vertical grid spacing	0.1–0.5 km			
	H = 12–25 km: fixed vertical grid spacing	0.5 km			

using a modified Smagorinsky-type scheme (horizturb = 1) with distinct mixing lengths in the radial (l_h = 750 m, constant) and vertical directions (asymptotes to l_{inf} = 100 m at $z = \infty$). The PBL parameterization scheme (ipbl = 2) is actually the same as the turbulence scheme. The upper-level Rayleigh damping is applied above z = 20 km, damping horizontal and vertical velocities toward the base state. The radiation scheme simply applies a constant cooling rate Q_{cool} = 1 K day^{-1} [Eq. (4) in CC20] to the potential temperature. This simple approach neglects all water–radiation and temperature–radiation feedbacks (Cronin and Chavas 2019). Dissipative heating is included. Sensitivity tests were performed with different horizontal or vertical mixing lengths and higher horizontal and vertical resolutions in addition to those summarized in Table 1, but simulation results are minimally sensitive to these choices (see Fig. 1 in the supplemental material).

We first run a 200-day baseline experiment that has an identical setup to that of CC20 using CM1v19.7. This baseline simulation allows a mature storm to reach a statistical steady-state, from which we identify a stable 15-day period, which starts at day 160 in this work. We then define the Control experiment (CTRL) as the ensemble-mean of five 10-day segments of the baseline experiment from this stable period whose start times are each one day apart. From each of the five CTRL ensemble member start times, we perform idealized landfall restart experiments by instantaneously modifying the surface evaporative fraction (ε) and surface drag coefficient (C_d) separately or jointly beneath the CTRL TC, each over a range of magnitudes or with different combinations as shown in Fig. 2. The five 10-day segments of each landfall experiments are then averaged into the experimental ensembles analogous to the CTRL. There is relatively little variability across ensemble members (supplementary Fig. 3), and using this ensemble approach helps to reduce noise and increases the robustness of the results. Surface wetness is modified by decreasing the surface evaporative fraction ε uniformly for simplicity, which reduces the surface latent heat fluxes F_{LH} through the decreased surface mixing ratio fluxes F_{qv} in CM1 (sfcphys.F). CM1 does not have an option to include sea spray physics (e.g., Andreas et al. 2015) and sea spray would no longer be relevant over land in landfall simulations, but this is something that could be explored in a more complex model. Surface roughness is modified by increasing the drag coefficient C_d, which modulates the surface roughness length z_0 and in turn the friction velocity u^* for the surface log-layer in CM1. Readers are referred to CC20 for full details of the modifications in CM1 experiments.

Notably, once the baseline simulation is spun-up, the short-term intensity response to different surface forcings are qualitatively identical across simulations restarting from different states of the baseline experiment. As shown in the supplementary Fig. 3a, we test identical landfall experiments during a nonequilibrium, size-decreasing period from day-40 ($v_{m,0}$ = 72.7 m s^{-1}), as well as a stable period with weaker initial intensity (day-75, $v_{m,0}$ = 65.4 m s^{-1}). The day-75 test produces a similar intensity response as the experiment restarting from the intense and stable period analyzed in this work (day-160). The lone significant difference is in the day-40 experiment, where $\tilde{v}_m$ in response to $4C_d$ does not exhibit the slight reintensification after $\tau > 40$ h found in the other experiments; this finding may be a great avenue to explore in future work but is beyond the scope of this paper. Here we simply test the theory against intensity responses from an equilibrium state.

Our experiments are summarized in Fig. 2. Roughening-only experiments ($2C_d$, $4C_d$, $6C_d$, $8C_d$, $10C_d$) and drying-only experiments (0.7ε, 0.5ε, 0.3ε, 0.25ε, 0.1ε) are fully introduced in CC20. The modification in C_d or ε yield systematic decreases in $\tilde{V}_p$ [Eq. (6)] across a similar range of values. For example, the 0.25ε and $4C_d$ experiments analyzed in detail in CC20 both have a similar value of $\tilde{V}_p \approx 0.5$. The combined experiments (gray boxes in Fig. 2) are simulated in the same manner but with the surface dried and roughened simultaneously. Our combined experiments are designed in a way where individual drying and roughening are systematically paired with each other; experiments are named by the corresponding modifications in C_d and ε. We focus on two specific subsets of experiments within this phase space. First, $0.7\varepsilon 2C_d$, $0.7\varepsilon 10C_d$, $0.1\varepsilon 2C_d$, and $0.1\varepsilon 10C_d$ (underlined in Fig. 2) are chosen as the representatives for extreme combinations, where each forcing takes its highest or lowest nonzero magnitude. Second, $0.5\varepsilon 2C_d$, $0.25\varepsilon 4C_d$, and $0.1\varepsilon 8C_d$ are chosen to represent cases where the individual forcing in a combined experiment yields similar contributions to $\tilde{V}_p$. Here we label $\tilde{V}_{p,\varepsilon}$, $\tilde{V}_{p,C_d}$, and $\tilde{V}_{p,\varepsilon C_d}$ of selected combined experiments in parentheses in Fig. 2. Finally, we generate a special set of combined experiments, $0V_pXC_d$, in which $\tilde{V}_p$ is fully reduced to zero for a range of magnitudes of roughening, which is achieved by setting both

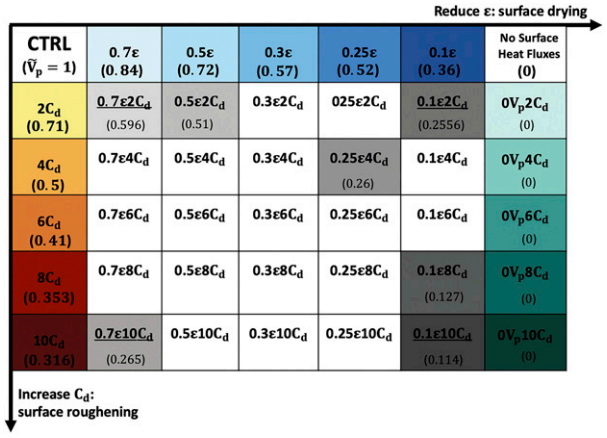

FIG. 2. Two-dimensional experimental phase space of surface drying (decreasing ε moving left to right) and surface roughening (increasing C_d moving top to bottom). CTRL is an ocean-like surface with $(C_d, \varepsilon) = (0.0015,1)$. Values of the potential intensity response $\tilde{V}_p$ for CTRL, individual drying or roughening, and representative combined experiments are listed in parentheses; $\tilde{V}_p$ for any combination of forcing is the product of $\tilde{V}_p$ for each individual forcing [Eq. (6)]. Experiments testing combined forcings are shaded gray and the subset testing the most extreme combinations of each forcing are underlined. Experiment set $0V_pXC_d$, corresponding to the special case where surface heat fluxes are entirely removed ($V_p = 0$), are shaded green.

surface sensible and latent heat fluxes to zero while increasing the roughness by a factor of X. This set of experiments all have $\tilde{V}_p = 0$ and are used to test the simplified form of E12 assuming $\tilde{v}_f = 0$ [Eq. (11)].

b. Testing theory against simulations

In each experiment, the simulated storm intensity $v_m(\tau)$ is normalized by the time-dependent, quasi-stable CTRL value, as $\tilde{v}_m(\tau)$, where τ denotes the time since the start of a given forcing experiment. We primarily focus on the first 36-h evolution, during which $\tilde{v}_m$ decreases monotonically across all roughening, drying, and combined experiments; this is also the time period of greatest practical relevance for real-world landfall. In addition, both the near-surface (10-m) intensity response $\tilde{v}_{m(10\text{m})}$ and above-BL (2-km) intensity response $\tilde{v}_{m(2\text{km})}$ are compared to theoretical predictions. The near-surface wind field is essential for predicting the inland TC hazards, while the theoretical solution is in principle formulated for the top of the boundary layer. We note though that E86 and E12 theory assumes a slab boundary layer where properties are uniform between the bottom and the top of the boundary layer, yet this theory also depends explicitly on the surface fluxes of enthalpy and momentum governed by the near-surface winds. As a result, the choice of the "correct" level for applying the theory to a height-varying boundary layer is ambiguous. Hence, we test the theoretical prediction against both $v_{m(2\text{km})}$ and $v_{m(10\text{m})}$. Peng et al. (2018) compares the 10-m simulated intensity with the diagnosed intensity using the underlying intensity equation in E12 though not the intensification solution [Eq. (8) itself]. Here we test this time-dependent intensity solution, similar to Emanuel (2018), but apply it to intensity decay. Over the ocean, $\tilde{v}_{m(10\text{m})}$ and $\tilde{v}_{m(2\text{km})}$ typically coevolve closely (Powell et al. 2003). However, at and after landfall, the response of near-surface winds is expected to deviate more strongly from the above-BL winds, particularly in the case of roughening, as found in CC20: there is a very rapid initial response of angular momentum (M) near the surface due to the enhanced frictional dissipation during the first 10 min that subsequently propagates upward as the vortex decays. The strengthened overturning circulation by Ekman adjustment transports reduced-M fluid near the surface inwards and then out of the boundary layer, thereby gradually spinning down the vortex aloft. In contrast, the response of angular momentum to surface drying initially occurs aloft in the eyewall due to the drying-induced eyewall stabilization. Then the response of M propagates into the boundary layer via the decreasing advective M transportation due to the weakened overturning circulation, though this response is generally slower and smoother in time. Therefore, it is practically useful to test intensity theories against both near-surface and above-BL winds.

For E86 theory, we first compare the simulated equilibrium intensity against the equilibrium E86 prediction of Eq. (6). We then compare the full time-dependent simulated intensity response against that predicted by assuming the total response is the product of the individual responses, $\tilde{v}^*(\tau)$ [Eq. (7)]. For E12 theory, we compare the simulated intensity evolution $\tilde{v}_m(\tau)$ against the E12 prediction $\tilde{v}_{m,\text{th}}(\tau)$ of Eqs. (10)–(11). In these solutions, the initial intensity $v_{m,\,0} = 95.4\,\text{m s}^{-1}$ for 2-km wind field and $v_{m,\,0} = 75.7\,\text{m s}^{-1}$ for 10-m wind field, respectively. The final intensity v_f in Eq. (10) is set as the minimum value of v_m during the first 5-day evolution in each experiment for simplicity. Using the actual simulated final intensity should implicitly account for deviations from the potential intensity due to additional complexities such as nongradient wind, at least as manifest in the v_f. Evaluating the role of gradient wind imbalance is an important avenue for future work. We further test a range of h for Eq. (10), which will be discussed in section 3c. For real-world landfalls, we do not know the minimum intensity prior to the inland evolution. Thus, as a final step, we compare simulation results against the theory with $\tilde{v}_f$ predicted from $\tilde{V}_p$. This final step may be useful for potentially applying the theory to real-world landfalls.

c. The boundary layer depth scale h

As introduced in section 2, h is uncertain both theoretically, as it is assumed to be constant, and in practice, because we do not have a simple mean of defining the boundary layer depth particularly during the landfall transition. Thus, we do not aim to resolve this uncertainty in h in the context of landfall, but rather we simply test what values of h provide the best predictions and evaluate to what extent variations in h across experiments align with variations in estimates of the boundary layer height H.

For each simulation, we test a range of constant values of h from 1.0 to 6.0 km in 0.1-km increments in order to identify a best-fit boundary layer depth scale, h_{BEST}. We define h_{BEST} as the value of h that produces the smallest average error throughout the first 36-h evolution for each

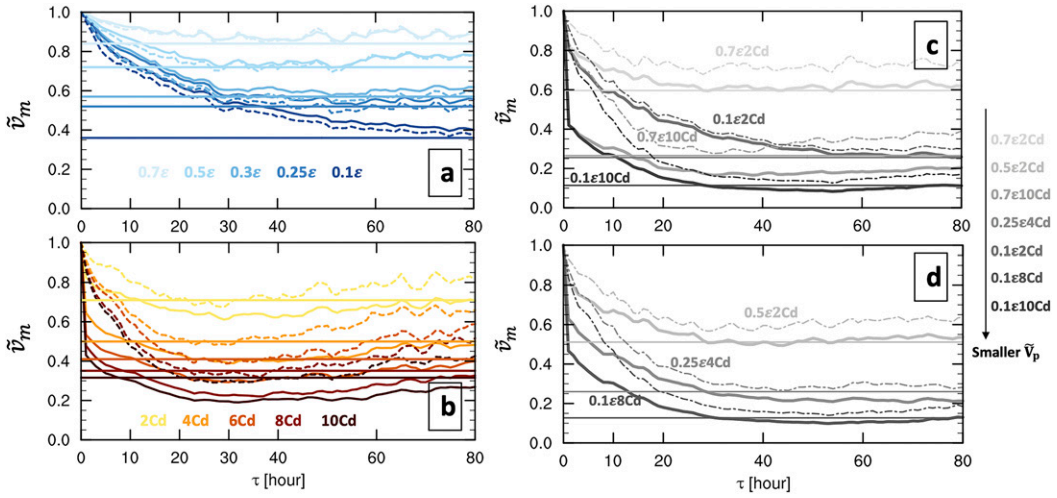

FIG. 3. Temporal evolution of simulated near-surface (10-m, solid curves) and above-BL (2-km, dash curves) $\tilde{v}_m$, across experiments: (a) surface drying, (b) surface roughening, and (c)–(d) representative combined experiments. Potential intensity response $\tilde{V}_p$ [Eqs. (4)–(6)] denoted by horizontal lines. Darker color indicates a smaller $\tilde{V}_p$.

experiment. We then compare the systematic variation in h_{BEST} against that of three typical estimates of boundary layer height H calculated from each simulation.

Since the E12 solution applies within the convecting eyewall region, we estimate H using three typical estimation methodologies and measure the value at the radius of maximum wind speed ($r_{\max}$) at the lowest model level: 1) H_{v_m} is the height of maximum tangential wind speed (Bryan and Rotunno 2009); 2) H_{inflow} is the height where radial wind u in the eyewall first decreases to 10% of its surface value (Zhang et al. 2011); and 3) H_{θ_v} is defined as the height where θ_v in the eyewall matches its value at the lowest model level (Seidel et al. 2010). The 36-h evolution of each estimate of H across our simulations is shown in supplementary Fig. 3. Because H varies in time during the experiments, the average value of H during τ = 0–6 h and τ = 30–36 h are each compared to the h_{BEST} to test whether there is a clearer relationship with its short-term versus long-term response.

4. Results

a. Near-surface versus above-BL intensity response

As discussed in section 3b, the simulated intensity responses near the surface (z = 10 m) and above the boundary layer (z = 2 km) may differ, and thus we intend to test the theory against both. We begin by simply identifying important differences between the intensity responses at each level.

For drying-only experiments, $\tilde{v}_{m(2\mathrm{km})}$ responds to reduced ε slightly faster than $\tilde{v}_{m(10\mathrm{m})}$ during the initial ~5 h (Fig. 3a), where stronger drying results in a larger deviation between the responses at each level during both the short-term and long-term evolution. In contrast, for roughening, $\tilde{v}_{m(10\mathrm{m})}$ responds nearly instantaneously across all roughening experiments, whereas $\tilde{v}_{m(2\mathrm{km})}$ responds more gradually. The magnitude of the deviation of $\tilde{v}_{m(10\mathrm{m})}$ from $\tilde{v}_{m(2\mathrm{km})}$ during the first 10 h increases with increasing roughening (Fig. 3b). Thereafter, $\tilde{v}_{m(10\mathrm{m})}$ and $\tilde{v}_{m(2\mathrm{km})}$ evolve at similar rates. This distinct behavior between the near-surface and 2-km wind response in each type of experiment is consistent with the findings of CC20, which showed that surface roughening has a significant and immediate impact on near-surface intensity while drying first impacts the eyewall aloft. Finally, as found in CC20, $\tilde{V}_p$ provides a reasonable prediction for the long-term equilibrium intensity response to each individual forcing; there is an overshoot in roughening experiments where $\tilde{v}_{m(10\mathrm{m})}$ reaches a minimum that is less than $\tilde{V}_p$ before gradually reintensifying toward $\tilde{V}_p$.

For our combined experiment sets (Figs. 3c–d), both surface drying and roughening determine the total response of storm intensity. However, regardless of the relative strength of each forcing, $\tilde{v}_{m(10\mathrm{m})}$ always decreases more rapidly than $\tilde{v}_{m(2\mathrm{km})}$ due to the surface roughening. Similar to the roughening-only experiment, stronger roughening results in a larger deviation of $\tilde{v}_{m(10\mathrm{m})}$ from $\tilde{v}_{m(2\mathrm{km})}$ during the first 20 h. Overall, the rapid initial response of near-surface intensity is controlled by the surface roughening regardless of the surface drying magnitude. Moreover, similar to the individual forcing experiments, $\tilde{V}_p$ provides a reasonable prediction for the simulated minimum $\tilde{v}_m$ in combined experiments. Notably, $\tilde{v}_m$ slightly reintensifies after reaching its minimum value for weak combined experiments ($0.7\varepsilon 2C_d$ and $0.5\varepsilon 2C_d$). This long-term reintensification also occurs in other experiments (Figs. 2a,b in CC20), the causes of which are unclear but is less relevant to our primary research questions with the regard to landfall. In this work, we focus on the first 36-h evolution during which the intensity decays monotonically in all three types of experiments.

b. Deconstructing simultaneous drying and roughening

Now we focus on the full time-dependent responses of the combined forcing experiments. We hypothesized based on traditional potential intensity theory [Eqs. (5)–(6)] that the transient response of storm intensity to simultaneous drying and roughening can be predicted as the product of their individual

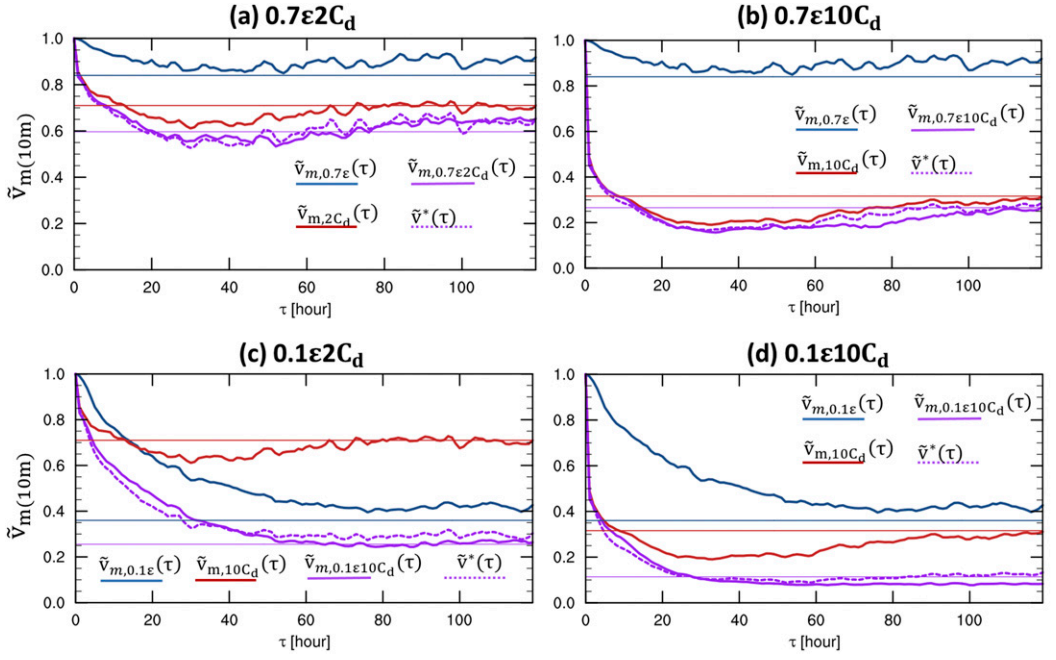

FIG. 4. Temporal evolution of simulated $\tilde{v}_m(\tau)$ for four representative combined experiments (solid purple) and their associated individual forcing experiments (solid blue for drying, solid red for roughening), with prediction $\tilde{v}^*(\tau)$ [dashed purple; Eq. (7)] defined as the product of the individual forcing responses. Horizontal line denotes $\tilde{V}_p$, colored by the corresponding experiment.

responses [Eq. (7)]. Thus, we compare the $\tilde{v}^*(\tau)$ to the simulated $\tilde{v}_m(\tau)$ of near-surface winds for our experiment set with extreme cases of combined drying and roughening (Fig. 4). Regardless of the magnitude of roughening and/or drying, $\tilde{v}^*(\tau)$ follows the simulated $\tilde{v}_m(\tau)$ closely through the initial rapid decay forced by roughening, the weakening stage through 36 h, and the final equilibrium stage. There is a slight low bias in $\tilde{v}^*(\tau)$ relative to the $\tilde{v}_m(\tau)$ throughout the primary weakening stage, especially for strong drying (Figs. 4c,d), indicating that there is a slight compensation in the response to roughening when strong drying is also applied. Overall, though, the full temporal evolution of the normalized responses to drying and roughening can indeed be combined multiplicatively. A very similar result is obtained for the above-BL intensity as well (not shown).

Although E86 theory is formulated for the equilibrium intensity, the above results indicate that the implication of its underlying physics also extends to the transient response to simultaneous surface drying and roughening. This behavior aligns with the notion that periods of intensity change represent a nonlinear transition of the TC system between two equilibrium stable attractors given by the preforcing and postforcing V_p (Kieu and Moon 2016; Kieu and Wang 2017). Because the distance between attractors is multiplicative, evidently so too is the trajectory between them.

c. Testing theory for transient intensity response

We next test the extent to which E12 theory [Eqs. (10) and (11)] can predict the intensity evolution, taking as input $\tilde{v}_f$ and a best-fit value of h_{BEST} from each simulation. The subsequent subsection compares the systematic variation in h_{BEST} against that of the three estimates of H in each set of experiments. Note that the $0.1\varepsilon 10C_d$ experiment is excluded in the following figures as it has a similar evolution as $0.1\varepsilon 8C_d$ (Figs. 3c,d).

We begin by focusing on the above-BL intensity. The E12-based solution [Eq. (10)] can reasonably capture the overall transient intensity response across all roughening, drying, and combined experiments (Figs. 5a–c). For drying-only experiments (Fig. 5a), the theory initially ($\tau < 5$ h) underestimates $\tilde{v}_{m(2\mathrm{km})}$ in 0.1ε experiment (Fig. 3a). h_{BEST} in drying experiments takes a value ranging 4–5 km and shows little systematic variations with increased drying magnitude (Fig. 5a). In contrast, h_{BEST} decreases with increased surface roughening, from 4.3 to 2.1 km (Fig. 5b). These results are consistent with the simulation results of Emanuel (2018) as introduced in section 2b. Here in surface drying experiments, though we keep C_k constant, the decreased ε reduces surface enthalpy fluxes, enhancing the intensity decay rate via $\tilde{v}_f$ in Eq. (14) in a manner that reproduces the simulated responses while h remains relatively constant [similar to Fig. 1 left in Emanuel (2012)]. In surface roughening experiments, the intensity decay rate increases with higher C_d as indicated by the decreasing trend in h_{BEST}, which is consistent with Emanuel (2018) (his Fig. 1 right) and Peng et al. (2018) (their Fig. 3b) for intensification with varying C_d. In the following subsection, we compare this variation in h_{BEST} to that of multiple estimates of H.

For the near-surface wind, E12 theory can capture the transient response of $\tilde{v}_m$ in drying experiments (Fig. 5d) using a similar h_{BEST}. For roughening and combined experiments, though, it misses the very rapid initial decay due to enhanced

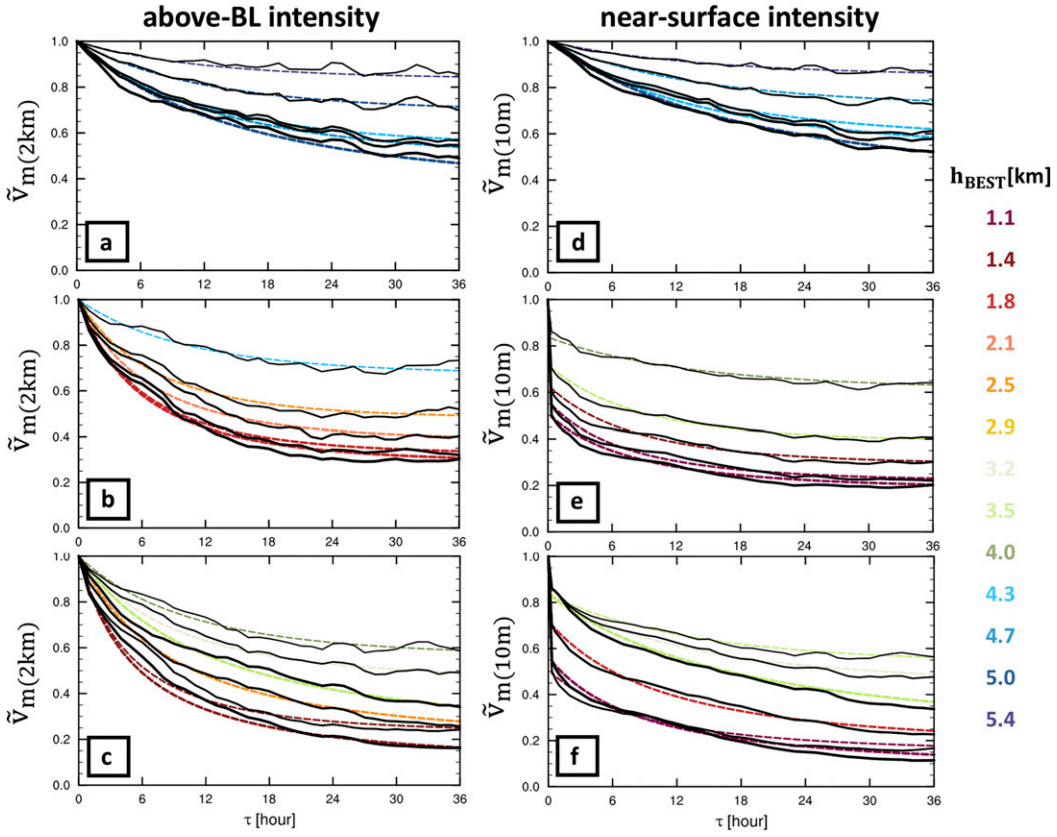

FIG. 5. (a)–(c) Temporal evolution of the simulated above-BL 2-km winds $\tilde{v}_m(\tau)$ (solid black) and theoretical prediction $\tilde{v}_{m,\mathrm{th}}(\tau)$ [dashed colored; Eq. (10)] for (a) drying, (b) roughening, and (c) combined experiments. $\tilde{v}_{m,\mathrm{th}}(\tau)$ is colored by the value of best-fit h, h_{BEST}. (d)–(f) As in (a)–(c), but for the near-surface 10-m winds, where the colored curves in (e) and (f) are the predictions from Eq. (14) to account for the initial rapid decay due to roughening.

C_d (Figs. 3b–d and 5e,f), which was shown in Fig. 1 of CC20 to occur within the first 10 min. The magnitude of this rapid initial decay depends on C_d, as surface roughening immediately removes momentum near the surface. To account for this initial response, we propose a simple model for this initial decay of $\tilde{v}_{m(10\mathrm{m})}$ that may be derived from the tangential momentum equation in a 1D slab boundary layer with a depth of h^*, given by

$$h^*\frac{dv}{dt} = -C_d|\mathbf{v}|v. \tag{12}$$

Taking $|\mathbf{v}| \approx v$, as $v \gg u$ in the eyewall, this equation may be integrated and then normalized by an initial intensity $v_{m,0}$ to yield

$$\tilde{v}_{m,\mathrm{th}}(\tau) = \left(\frac{C_d v_{m,0}}{h^*}\tau + 1\right)^{-1}. \tag{13}$$

Curiously, Eq. (13) is mathematically identical to the E12 solution with $v_f = 0$ [Eq. (11)] except with C_k replaced by $2C_d$, a topic we return to in the conclusions.

We may combine Eq. (13) for the first 10-min evolution with Eq. (10) to model the complete near-surface intensity response to surface roughening:

$$\tilde{v}_{m,\mathrm{th}}(\tau) = \begin{cases} \left(\dfrac{C_d v_{m,0}}{h^*}\tau + 1\right)^{-1} & \tau \le 10\,\mathrm{min} \\ \tilde{v}_f \coth\left[\dfrac{C_k v_f}{2h}(\tau - 600\,\mathrm{s}) + \tanh^{-1}(\tilde{v}_f^*)\right] & \tau > 10\,\mathrm{min}, \end{cases} \tag{14}$$

where $\tilde{v}_f^* = v_f/v_{m,\mathrm{th}}(10\,\mathrm{min})$ since $v_{m,\mathrm{th}}$ now decreases from a new initial intensity $v_{m,\mathrm{th}}(10\,\mathrm{min})$ calculated from the first equation. For the $\tau \le 10$ min solution, we find that the rapid decay by $\tau = 10$ min across all roughening experiments can be captured by setting $h^* = 0.7$ km constant, which yields a constant decay rate during the period $\tau = 0$–10 min. In reality, the decay rate is very large in the first minute and monotonically decreases through the 10-min period. This time-varying decay rate can be reproduced by allowing h^* to increase with time from an initial very small value, which aligns with the physical response to roughening that may be thought of as the formation of a new internal boundary layer that begins at the surface and rapidly expands upward. Here though we employ a constant h^* in order to retain a simple analytic solution; the 10-min period is short enough that the difference is likely not of practical significance. Thereafter, we estimate h_{BEST} for each simulation in the same manner as before.

The comparison of model against simulations is shown in Figs. 5e,f. Equation (14) can capture the simulated near-surface transient intensity response $\tilde{v}_m(\tau)$ across roughening and combined experiments. The trend of $h_{\rm BEST}$ for the prediction of $\tilde{v}_{m(10\rm m)}$ are similar to those obtained for the above-BL case but slightly smaller in magnitude (Figs. 5b,e,c,f).

Similar behavior associated with roughening is found in experiments for the special case $v_f = 0$ (Fig. 6). Thus, we again propose a two-stage model for $\tilde{v}_{mm(10\rm m)}$ given by

$$\tilde{v}_{m,\rm th}(\tau) = \begin{cases} \left(\dfrac{C_d v_{m,0}}{h^*}\tau + 1\right)^{-1} & \tau \le 10\,\text{min} \\ \left(\dfrac{C_k v_{m,0}}{2h}(\tau - 600\,\text{s}) + v^*_{m,0}\right)^{-1} & \tau > 10\,\text{min}, \end{cases} \tag{15}$$

where $v^*_{m,0} = v_{m,0}/[v_{m,\rm th}(\tau = 10\,\text{min})]$. The comparison of model against simulations is shown in Fig. 6, where $h_{\rm BEST}$ exhibits a decreasing trend with enhanced surface roughening, similar to that found in the pure roughening experiments.

Note that multiplying both sides of Eq. (12) by v yields a budget equation for kinetic energy given by $h[d(\text{KE})/dt] = -C_d v^3$, where $\text{KE} = (1/2)v^2$ and the RHS is the expression for surface frictional dissipation of kinetic energy that is standard in TC theory (Bister and Emanuel 1998; Tang and Emanuel 2010; Chavas 2017).[1] Physically, then, the solution for the initial roughening response represents the intensity response to the dominant sink of kinetic energy in the absence of the dominant compensating thermodynamic source of kinetic energy from surface heat fluxes for a tropical cyclone. After this initial response, the trajectory follows a solution that accounts for both source and sink as encoded in E12 theory. The interpretation is that there exists a brief initial period where surface roughening directly modifies the near-surface air in a manner that is thermodynamically independent of the rest of the vortex. Thereafter, the vortex has adjusted, and weakening proceeds according to processes governed by the full TC system, analogous to that of drying. In reality this transition is likely not instantaneous, though we have modeled it as so here for simplicity. The details of this adjustment process warrant more in-depth investigation that is beyond the scope of this work.

Comparing the variation of $h_{\rm BEST}$ and estimates of H

We next compare the variations of $h_{\rm BEST}$ from our simulations to that of three common estimates of the boundary layer height: H_{v_m}, $H_{\rm inflow}$, and H_{θ_v}. We compare trends for both the initial response (0–6 h) and the equilibrium response (30–36 h) (Figs. 7d–f). As noted above, $h_{\rm BEST}$ was found to decrease with increased roughening (Fig. 7a) but remain relatively constant for increased drying (Fig. 7b). Moreover, $h_{\rm BEST}$ values are quite similar when estimated from the above-BL versus near-surface responses (Figs. 7a–c), and hence this discussion is not dependent on the choice of level for defining $h_{\rm BEST}$.

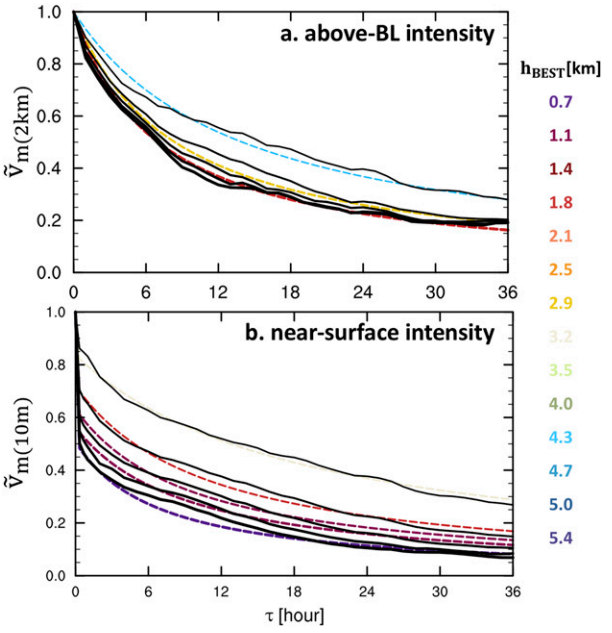

FIG. 6. Temporal evolution of simulated intensity response (solid black) and theoretical prediction (dashed colored) for the experiment set $0V_pXC_d$: (a) above-BL 2-km winds [Eq. (11)], where the E12 prediction for $0V_p4C_d$ and $0V_p6C_d$ (yellow) and $0V_p8C_d$and $0V_p10C_d$ (red) are overlapping each other since they share the same $h_{\rm BEST}$ (Fig. 7c). (b) As in (a), but for near-surface 10-m winds [Eq. (15)]. E12-based prediction is colored by the value of $h_{\rm BEST}$ for corresponding experiment.

To show the variation of estimates of H in different sets of experiments, we normalize each H by its corresponding value in the CTRL experiment as $H_{\rm exp}/H_{\rm CTRL}$ (Figs. 7d–f), where each estimate of H in the CTRL experiment is quasi-stable (supplementary Fig. 4). We focus first on the responses to pure roughening or pure drying (Fig. 7, top two rows). During 0–6 h, all three estimates of H slightly increase with enhanced roughening and are approximately constant with enhanced drying (Figs. 7d–f, color). By 30–36 h, H decreases with enhanced roughening and enhanced drying for H_{v_m} and $H_{\rm inflow}$, while H_{θ_v} remains relatively constant for each (Figs. 7d–f, shaded).

Overall, there is no single estimate of H whose systematic variation matches that of $h_{\rm BEST}$ (Fig. 7). For roughening-only experiments, the initial response of all three estimates of H with enhanced roughening is opposite to that of $h_{\rm BEST}$ (Figs. 7a,d), though the slow response of each H for two of the estimates does show a decrease with enhanced roughening (Fig. 7d, shaded). For drying-only experiments, the initial response of H is either constant or very slowly decreasing with enhanced drying (Figs. 7b,e), similar to $h_{\rm BEST}$. However, the slow response of H_{v_m} and $H_{\rm inflow}$ decreases with enhanced drying in contrast to the nearly constant $h_{\rm BEST}$, while the slow response of H_{θ_v} is again relatively constant (Fig. 7e, shaded).

Finally, for $0V_pXC_d$ experiments (Fig. 6), $h_{\rm BEST}$ exhibits a similar systematic response to enhanced surface roughening as

[1] The KE budget equation may be expressed as $h[d(\text{KE})/dt] = -2C_d|\mathbf{v}|(\text{KE})$. Hence, $2C_d$ represents the surface exchange coefficient of kinetic energy over a static surface.

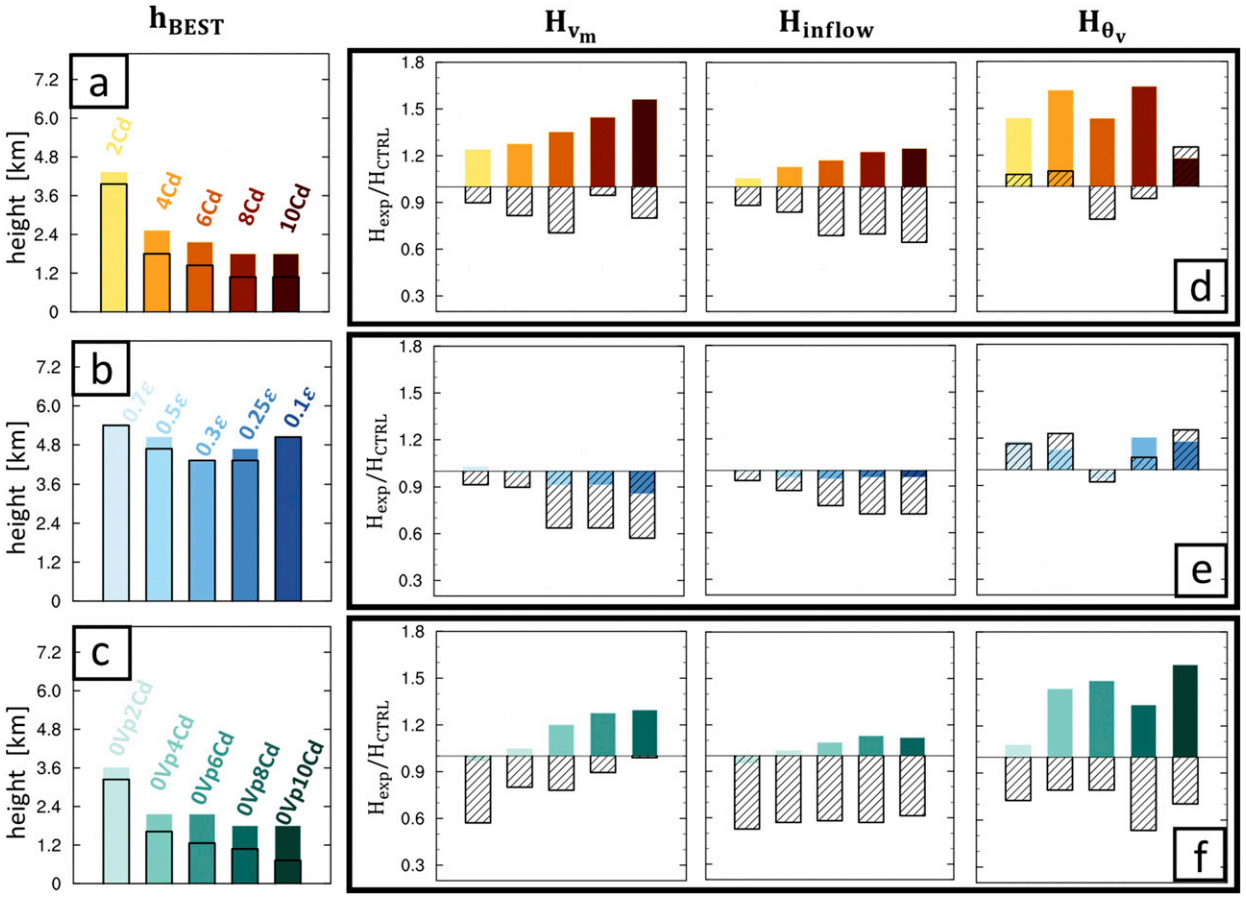

FIG. 7. Comparison of (a)–(c) h_{BEST} and(d)–(f) the systematic variation of three estimates of boundary layer height H for each set of surface roughening, surface drying, and $0V_pXC_d$ experiments. For (a)–(c), h_{BEST} is shown for the above-BL (color) and near-surface (box) intensity predictions. For (d)–(f), H_{exp}/H_{CTRL} is shown for the early period (τ = 0–6 h; color) and later period (τ = 30–36 h; hatched box). The CTRL values of H_{v_m}, H_{inflow}, and H_{θ_v} are 0.9, 1.55, and 0.64 km, respectively.

the pure roughening experiments (Figs. 7a,c). Turning off all heat fluxes does not significantly alter the variation of h_{BEST} with roughening relative to the pure-roughening experiments; this behavior is also similar to the pure drying experiments where h_{BEST} remains constant with enhanced drying. The systematic variation in h_{BEST} disagrees with both the fast and the slow response of all three estimates of H (Figs. 7c,f). Prediction errors of the model prediction using estimates of H to define h for each experiment is shown in supplementary Fig. 5.

Note that for the combined experiments, there is no clear evidence to link the decreasing trend in h_{BEST} (Figs. 5c,f) to the change in each individual forcing. Thus, we elect not to speculate on the details of h_{BEST} and H for the combined experiments; instead, in the next section we explore a more practical theoretical prediction for combined forcing cases that applies h_{BEST} to drying and roughening experiments individually.

The disagreement in the systematic trends both among estimates of H and between each estimate of H and h_{BEST} highlights the need for more detailed studies on the TC boundary layer during and after landfall in future work. In terms of E12 theory, though the solution can reproduce the decay evolution, it also likely oversimplifies the TC boundary layer, where a constant h cannot fully capture the time- and the radially varying response of boundary layer height to landfall-like surface forcing. In terms of boundary layer theory, the optimal definition of boundary layer depth is itself uncertain. Meanwhile, without a comprehensive understanding of the TC boundary layer during landfall, it is unclear if one particular definition of H, if any, might be most appropriate for E12 theory within the eyewall. Therefore, having a better estimation of h in the E12 solution and an improved understanding of boundary layer evolution during and after landfall would help explain the differences in systematic variations between h and estimates of H.

d. Predicting the intensity response combining equilibrium and transient theory

We may combine all theoretical findings presented above to predict the near-surface intensity response to idealized landfalls for experiments combining drying and roughening. This represents the most complex of our experimental outcomes.

We begin from the result of Eq. (7) and predict the intensity response to simultaneous surface drying and roughening as the product of their individual predicted intensity responses:

$$\tilde{v}_{\mathrm{th}(C_d\varepsilon)} \approx \tilde{v}^*_{\mathrm{th}} = \tilde{v}_{\mathrm{th}(C_d)}\tilde{v}_{\mathrm{th}(\varepsilon)}, \tag{16}$$

where $\tilde{v}_{\mathrm{th}(\varepsilon)}$ is generated by Eq. (10) and $\tilde{v}_{\mathrm{th}(C_d)}$ is generated by Eq. (14). When applying the transient solution for each individual forcing component, we use the previously identified h_{BEST} from Figs. 7a and 7b and predict the $\tilde{v}_f$ using $\tilde{V}_p$ given by Eqs. (4) and (5). In principle, an empirical model for h_{BEST} for each individual forcing could be generated from our data since h_{BEST} is approximately constant with enhanced drying and monotonically decreasing with enhanced roughening. But given the uncertainties in h_{BEST} as a true physical parameter, we elect not to take such a step here.

The results are shown in Fig. 8. Overall, our analytic theory performs well in capturing the first-order response across experiments, particularly given the relative simplicity of the method. Therefore, given estimates of $\tilde{V}_p$ and h_{BEST}, one can generate a theoretical time-dependent intensity response prediction for any combination of uniform surface forcing. This offers an avenue to link our theoretical understanding to real-world landfalls.

e. *Comparison with existing empirical decay model*

Finally, as a first step toward linking theory and real-world landfalls, we provide a simple comparison of our theoretical model with the prevailing empirical model for inland decay. The model was first introduced by DeMaria and Kaplan (1995) and most recently applied to historical observations by Jing and Lin (2019) as

$$V(t) = V_b + (V_0 - V_b)e^{-\alpha t}, \tag{17}$$

where storm landfall intensity V_0 decays to a background intensity V_b with a constant exponential decay rate α. Jing and Lin (2019) estimated $V_b = 18.82\,\mathrm{kt}$ ($9.7\,\mathrm{m\,s^{-1}}$) and $\alpha = 0.049\,\mathrm{h^{-1}}$ using the historical Atlantic hurricane database.

Comparisons between theory and Eq. (17) predictions are shown in Fig. 9, for a range of V_0 from 100 to $23\,\mathrm{m\,s^{-1}}$, similar to Jing and Lin (2019) (their Fig. 3). Given that TCs in nature eventually dissipate (and typically do so rapidly), we choose the theoretical equation with $v_f = 0$ [Eq. (11)]; this is also by far the simplest choice since no final intensity information is required at all. We set $h = 5\,\mathrm{km}$ constant. Equation (11) compares well against the empirical prediction for inland intensity decay, capturing the first-order structure of the characteristic response found in real-world storms. Mathematically, for a weaker storm (smaller $v_{m,0}$), the fit across intensities over the first day or two can be improved by using a smaller constant h applied in Eq. (11), but a physical explanation for this trend is not clear. Note that the temporal structure of the empirical model is constrained strongly by its assumed exponential form, so differences beyond the gross structure should not be overinterpreted. Ultimately, the consistency with the empirical model provides additional evidence that the physical model may indeed be applicable to the real world. Hence, it may provide a foundation to develop a physically based understanding of the evolution of the TC after landfall.

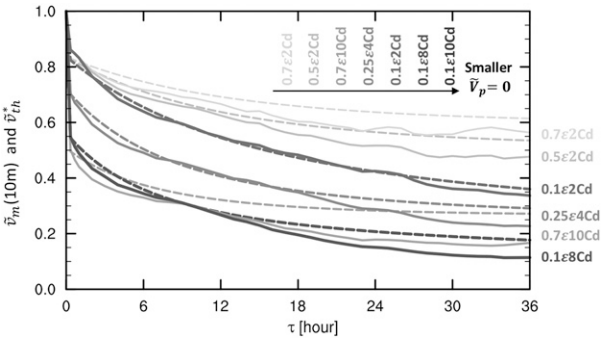

FIG. 8. Temporal evolution of simulated near-surface intensity response for combined forcing experiments (solid) and the corresponding prediction combining the equilibrium and transient theory [dashed; Eq. (16)], with $\tilde{v}_f = \tilde{V}_p$ and setting h equal to the values of h_{BEST} for the individual predicted responses to drying [Eq. (10)] and roughening [Eq. (14)].

5. Summary

This work tests the extent to which equilibrium and transient tropical cyclone intensity theory, the latter reformulated here to apply to inland intensity decay, can predict the simulated equilibrium and transient intensity response of a mature tropical cyclone to surface drying, roughening, and their combination. This work builds off of the mechanistic study of Chen and Chavas (2020) that analyzed the responses of a mature tropical cyclone to these surface forcings applied individually. Key findings are as follows:

- The transient response of storm intensity to any combination of surface drying and roughening is well captured as the product of the response to each forcing individually [Eq. (7)]. That is, the time-dependent intensity evolution in response to a land-like surface can be understood and predicted via deconstructed physical processes caused by individual surface roughening and drying. Surface roughening imposes a strong and rapid initial response and hence dominates decay within the first few hours regardless of the magnitude of drying.
- The equilibrium response of storm intensity to simultaneous surface drying and roughening is well predicted by traditional potential intensity theory [Eq. (6)].
- The transient response of storm intensity to drying and roughening can be predicted by the intensification theory of Emanuel (2012), which has been generalized to apply to weakening in this work [Eq. (10)], though with variations in the depth scale h that lack a clear explanation. This theory predicts an intensity decay to a final, weaker equilibrium that can be estimated by Eq. (6). The intensity prediction also depends on the boundary layer depth scale h, whose best-fit values are comparable to the value used in E12. Systematic trends of h to surface forcings do not clearly match commonly defined TC boundary layer height.

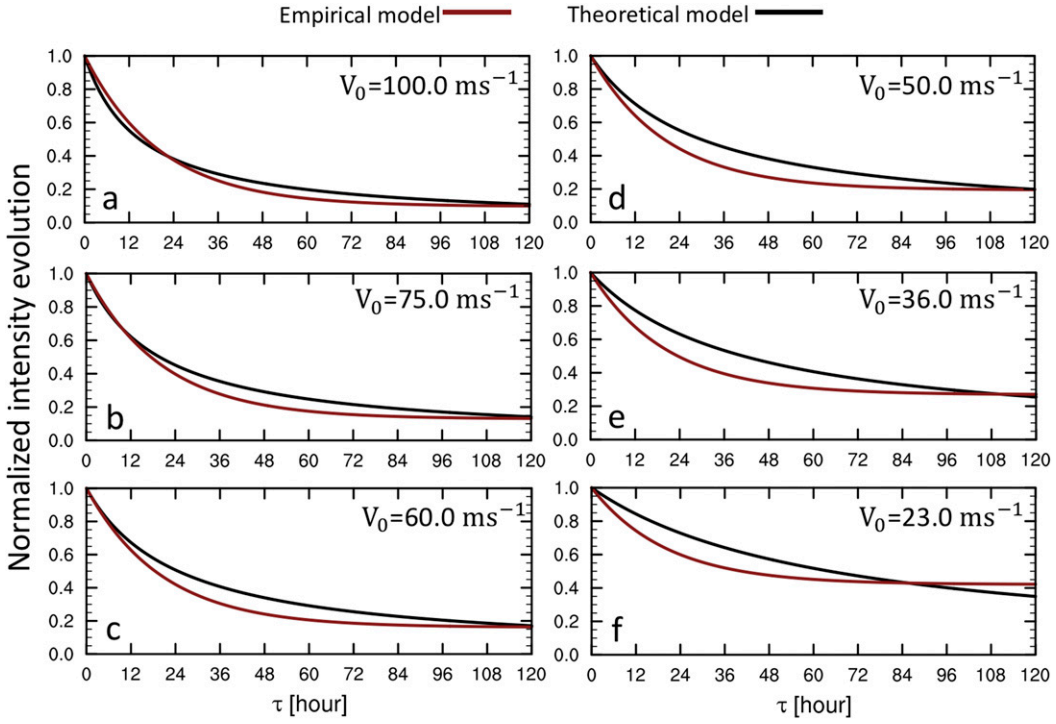

FIG. 9. Comparison between the theoretical intensity prediction for $v_f = 0$ [Eq. (11)] against the prevailing empirical exponential decay model prediction from Jing and Lin (2019) [Eq. (17)] for a range of initial intensities [(100, 75, 60, 50, 36, 23) m s^{-1}]. For comparison with theory, Eq. (17) is normalized by the initial intensity V_0. For the theoretical prediction, $h = 5$ km.

- An additional modification is required to model the near-surface (10-m) response specifically for surface roughening, which induces a rapid initial decay for near-surface intensity during the first 10 min. The magnitude of this initial rapid response increases with enhanced roughening and can be modeled analytically as a pure frictional spindown [Eqs. (13) and (14)].
- The above findings about the transient and equilibrium responses can be applied together to generate a theoretical prediction for the time-dependent intensity response to any combination of simultaneous surface drying and roughening [Eq. (16)]. This prediction compares reasonably well against simulation experiments with both surface forcings.
- In the special case where the final equilibrium intensity is taken to be zero, the E12 solution reduces to a simpler analytic form that depends only on initial intensity and boundary layer depth scale [Eq. (11)]. This solution is found to compare well against experiments with surface fluxes turned off for a range of magnitudes of surface roughening. This solution is perhaps most directly analogous to the real world, and it is found to compare well with the prevailing empirical model for landfall decay [Eq. (17)] across a range of initial intensities.

Although existing intensity theories are formulated for the tropical cyclone over the ocean, the above findings suggest that those underlying physics may also be valid in the postlandfall storm evolution. Note that we have not systematically tested the underlying assumptions of the theory but have focused on testing the performance of theories for predicting the response to idealized landfalls. The principal result is that for an idealized landfall, one can generate a reasonable prediction for the time-dependent intensity evolution if the inland surface properties along the TC track are known.

Landfall in the real world is certainly much more complicated. The real world has substantial horizontal variability in surface properties compared to idealized landfalls where the surface roughness and wetness beneath the storm are instantaneously and uniformly modified. Additional environmental variability during the transition, including heterogeneity in surface temperature and moisture, environmental stratification, topography, land–atmosphere feedbacks, vertical wind shear, and translation speed, is excluded in these idealized simulations. Therefore, a theoretical prediction for the first-order intensity response to major postlandfall surface forcings in an idealized setting provides a foundation for understanding TC landfall in nature. In this vein, our results suggest that the TC landfall process could plausibly be deconstructed into transient responses to individual surface and/or environmental forcings as encoded in our existing theories. Here individual surface drying and roughening each act to reduce the potential intensity. Changes in other surface properties found in Eq. (1), including the surface temperature T_{ST}, tropopause temperature T_{tpp}, and surface sensible heat fluxes $C_p\Delta T$, may further modulate the potential intensity response. Future work may seek to test these additional factors using the experimental framework presented here. One implication of this work is the

potential to predict how postlandfall intensity decay may change in a changing climate if we know how each surface forcing will change in the future (Zeng and Zhang 2020). Theoretical solutions presented in this work may also be of use in risk models for hazard prediction.

In terms of theory, future work may seek to test the theory against simulations in three-dimensional and/or coupled models that include additional complexities. That said, several questions pertinent to axisymmetric geometry remain open here: do changes in surface sensible heat fluxes significantly alter the response to surface drying? How might changes in C_k, whose variation after landfall is not known, alter the results? How should one optimally define TC boundary layer height for the convective eyewall region where boundary layer air rises rapidly into updrafts, both in general and in the context of the transition from ocean to land? How best can this be used to approximate the boundary layer depth scale h in the theoretical solution?

We note that the solution for pure frictional spindown [Eq. (13)] and the E12 solution for zero final intensity [Eq. (11)] have an identical mathematical form, with the lone difference being trading the parameter C_k for $2C_d$. These are simply the exchange coefficients for the dominant kinetic energy source (enthalpy fluxes) and sink (frictional dissipation) for the TC, respectively. Physically, we interpreted these two solutions as found in our work as a transition from a rapid response governed by pure frictional spindown to a response governed by the reintroduction of the counterbalancing thermodynamic source of energy for the tropical cyclone as encoded in Emanuel (2012) theory (and similarly in traditional time-dependent Carnot-based theory). More generally, though, why should the large difference in the underlying physics of these two regimes manifest itself mathematically as a simple switch in exchange coefficients? This is curious.

Finally, future work may seek to test these theoretical predictions against observations accounting for variations in surface properties. Here we showed that our physically based model appears at least broadly consistent with the prevailing empirical exponential decay model, suggesting that our model may provide an avenue for explaining variability in decay rates both spatially and temporally, including across climate states. For example, theory may be useful to understand how surface properties facilitate those rare TCs that do not weaken after landfall (Evans et al. 2011; Andersen and Shepherd 2013). This would help us link physical understanding to real-world landfalls, which is important for improving the modeling of inland hazards.

Acknowledgments. The authors thank for all conversations and advice from Frank Marks, Jun Zhang, and Xiaomin Chen on the hurricane boundary layer. The authors were supported by NSF Grants 1826161 and 1945113. We also appreciate the feedback and conversations related to this research during the 101thAGUFall Meeting and the 101st AMS Annual Meeting. Finally, we thank two anonymous reviewers for their constructive feedback that improved this manuscript.

Data availability statement. The full outputs of the numerical model simulations upon which this study is based are too large to archive or to transfer. Instead, we provide all the simulated variables applied in this work on Purdue University Research (PURR) available at https://purr.purdue.edu/, including the model code, compilation script, and the namelist settings needed to replicate the simulations.

APPENDIX

Generalizing the Emanuel (2012) Intensification Solution

The E12-based decay solution is derived from Eq. (17) of Emanuel (2012), given by

$$\frac{\partial v_m}{\partial \tau} = \frac{C_k}{2h}(v_f^2 - v_m^2), \tag{A1}$$

where v_m is the initial intensity (maximum tangential wind speed) and v_f is defined as the theoretical steady-state maximum intensity. However, v_f need not be larger than the current intensity but rather may be generalized to any final quasi-steady intensity, larger or smaller. Integrating Eq. (A1) yields the following:

$$\int \frac{1}{v_f^2 - v_m^2} dv_m = \int \frac{C_k}{2h}\, d\tau, \tag{A2}$$

$$\frac{\ln|v_m + v_f| - \ln|v_m - v_f|}{2v_f} = \frac{C_k}{2h}\tau + C, \tag{A3}$$

$$\frac{|v_m + v_f|}{|v_m - v_f|} = e^{[2(C_k v_f/2h)\tau + C]}. \tag{A4}$$

Ramsay et al. (2020) showed that for intensification where $v_m < v_f$, the solution is

$$v_{m,\mathrm{th}}(\tau) = v_f \tanh\left[\frac{C_k v_f}{2h}\tau + \coth^{-1}\left(\frac{v_f}{v_{m,0}}\right)\right]. \tag{A5}$$

Equation (A5) reduces to Eq. (19) of Emanuel (2012) when the initial intensity $v_{m,0} = 0$, for which $\coth^{-1}(v_f/0) = 0$.

Alternatively, for decay where $v_f < v_m$, the solution is

$$v_{m,\mathrm{th}}(\tau) = v_f \coth\left[\frac{C_k v_f}{2h}\tau + \tanh^{-1}\left(\frac{v_f}{v_{m,0}}\right)\right]. \tag{A6}$$

Equation (A6) may be normalized by $v_{m,0}$ to define the intensity response relative to the initial intensity given by Eq. (10) in the main text.

REFERENCES

Alford, A. A., J. A. Zhang, M. I. Biggerstaff, P. Dodge, F. D. Marks, and D. J. Bodine, 2020: Transition of the hurricane boundary layer during the landfall of Hurricane Irene (2011). *J. Atmos. Sci.*, **77**, 3509–3531, https://doi.org/10.1175/JAS-D-19-0290.1.

Andersen, T., and J. M. Shepherd, 2013: A global spatiotemporal analysis of inland tropical cyclone maintenance or intensification. *Int. J. Climatol.*, **34**, 391–402, https://doi.org/10.1002/joc.3693.

Andreas, E. L, L. Mahrt, and D. Vickers, 2015: An improved bulk air–sea surface flux algorithm, including spray-mediated transfer. *Quart. J. Roy. Meteor. Soc.*, **141**, 642–654, https://doi.org/10.1002/qj.2424.

Bhowmik, S. K. R., S. D. Kotal, and S. R. Kalsi, 2005: An empirical model for predicting the decay of tropical cyclone wind speed after landfall over the Indian region. *J. Appl. Meteor.*, **44**, 179–185, https://doi.org/10.1175/JAM-2190.1.

Bister, M., and K. E. Emanuel, 1998: Dissipative heating and hurricane intensity. *Meteor. Atmos. Phys.*, **65**, 233–240, https://doi.org/10.1007/BF01030791.

Bryan, G. H., 2012: Effects of surface exchange coefficients and turbulence length scales on the intensity and structure of numerically simulated hurricanes. *Mon. Wea. Rev.*, **140**, 1125–1143, https://doi.org/10.1175/MWR-D-11-00231.1.

——, and J. M. Fritsch, 2002: A benchmark simulation for moist nonhydrostatic numerical models. *Mon. Wea. Rev.*, **130**, 2917–2928, https://doi.org/10.1175/1520-0493(2002)130<2917:ABSFMN>2.0.CO;2.

——, and R. Rotunno, 2009: The maximum intensity of tropical cyclones in axisymmetric numerical model simulations. *Mon. Wea. Rev.*, **137**, 1770–1789, https://doi.org/10.1175/2008MWR2709.1.

Chavas, D. R., 2017: A simple derivation of tropical cyclone ventilation theory and its application to capped surface entropy fluxes. *J. Atmos. Sci.*, **74**, 2989–2996, https://doi.org/10.1175/JAS-D-17-0061.1.

Chen, J., and D. R. Chavas, 2020: The transient responses of an axisymmetric tropical cyclone to instantaneous surface roughening and drying. *J. Atmos. Sci.*, **77**, 2807–2834, https://doi.org/10.1175/JAS-D-19-0320.1.

Cosby, B. J., G. Hornberger, R. B. Clapp, and T. Ginn, 1984: A statistical exploration of the relationships of soil moisture characteristics to the physical properties of soils. *Water Resour. Res.*, **20**, 682–690, https://doi.org/10.1029/WR020i006p00682.

Cronin, T. W., and D. R. Chavas, 2019: Dry and semidry tropical cyclones. *J. Atmos. Sci.*, **76**, 2193–2212, https://doi.org/10.1175/JAS-D-18-0357.1.

Davis, C. A., and Coauthors, 2008: Prediction of landfalling hurricanes with the Advanced Hurricane WRF Model. *Mon. Wea. Rev.*, **136**, 1990–2005, https://doi.org/10.1175/2007MWR2085.1.

DeMaria, M., and J. Kaplan, 1994: Sea surface temperature and the maximum intensity of Atlantic tropical cyclones. *J. Climate*, **7**, 1324–1334, https://doi.org/10.1175/1520-0442(1994)007<1324:SSTATM>2.0.CO;2.

——, and ——, 1995: A simple empirical model for predicting the decay of tropical cyclone winds after landfall. *J. Appl. Meteor.*, **34**, 2499–2512, https://doi.org/10.1175/1520-0450(1995)034<2499:ASEMFP>2.0.CO;2.

——, M. Mainelli, L. K. Shay, J. A. Knaff, and J. Kaplan, 2005: Further improvements to the Statistical Hurricane Intensity Prediction Scheme (SHIPS). *Wea. Forecasting*, **20**, 531–543, https://doi.org/10.1175/WAF862.1.

——, J. A. Knaff, and J. Kaplan, 2006: On the decay of tropical cyclone winds crossing narrow landmasses. *J. Appl. Meteor. Climatol.*, **45**, 491–499, https://doi.org/10.1175/JAM2351.1.

Duran, P., and J. Molinari, 2018: Dramatic inner-core tropopause variability during the rapid intensification of Hurricane Patricia (2015). *Mon. Wea. Rev.*, **146**, 119–134, https://doi.org/10.1175/MWR-D-17-0218.1.

Emanuel, K. A., 1986: An air-sea interaction theory for tropical cyclones. Part I: Steady-state maintenance. *J. Atmos. Sci.*, **43**, 585–605, https://doi.org/10.1175/1520-0469(1986)043<0585:AASITF>2.0.CO;2.

——, 1997: Some aspects of hurricane inner core dynamics and energetics. *J. Atmos. Sci.*, **54**, 1014–1026, https://doi.org/10.1175/1520-0469(1997)054<1014:SAOHIC>2.0.CO;2.

——, 2012: Self-stratification of tropical cyclone outflow. Part II: Implications for storm intensification. *J. Atmos. Sci.*, **69**, 988–996, https://doi.org/10.1175/JAS-D-11-0177.1.

——, 2018: Corrigendum. *J. Atmos. Sci.*, **75**, 2155–2156, https://doi.org/10.1175/JAS-D-18-0047.1.

——, and R. Rotunno, 2011: Self-stratification of tropical cyclone outflow. Part I: Implications for storm structure. *J. Atmos. Sci.*, **68**, 2236–2249, https://doi.org/10.1175/JAS-D-10-05024.1.

——, S. Ravela, E. Vivant, and C. Risi, 2006: A statistical deterministic approach to hurricane risk assessment. *Bull. Amer. Meteor. Soc.*, **87**, 299–314, https://doi.org/10.1175/BAMS-87-3-299.

Evans, C., R. S. Schumacher, and T. J. Galarneau, 2011: Sensitivity in the overland reintensification of Tropical Cyclone Erin (2007) to near-surface soil moisture characteristics. *Mon. Wea. Rev.*, **139**, 3848–3870, https://doi.org/10.1175/2011MWR3593.1.

Jin, J., N. L. Miller, and N. Schlegel, 2010: Sensitivity study of four land surface schemes in the WRF model. *Adv. Meteor.*, **2010**, 167436, https://doi.org/10.1155/2010/167436.

Jing, R., and N. Lin, 2019: Tropical cyclone intensity evolution modeled as a dependent hidden Markov process. *J. Climate*, **32**, 7837–7855, https://doi.org/10.1175/JCLI-D-19-0027.1.

——, and ——, 2020: An environment-dependent probabilistic tropical cyclone model. *J. Adv. Model. Earth Syst.*, **12**, e2019MS00197, https://doi.org/10.1029/2019MS001975.

Kaplan, J., and M. DeMaria, 1995: A simple empirical model for predicting the decay of tropical cyclone winds after landfall. *J. Appl. Meteor. Climatol.*, **34**, 2499–2512, https://doi.org/10.1175/1520-0450(1995)034<2499:ASEMFP>2.0.CO;2.

——, and ——, 2001: On the decay of tropical cyclone winds after landfall in the New England area. *J. Appl. Meteor.*, **40**, 280–286, https://doi.org/10.1175/1520-0450(2001)040<0280:OTDOTC>2.0.CO;2.

Kepert, J. D., 2001: The dynamics of boundary layer jets within the tropical cyclone core. Part I: Linear theory. *J. Atmos. Sci.*, **58**, 2469–2484, https://doi.org/10.1175/1520-0469(2001)058<2469:TDOBLJ>2.0.CO;2.

——, 2010: Slab- and height-resolving models of the tropical cyclone boundary layer. Part I: Comparing the simulations. *Quart. J. Roy. Meteor. Soc.*, **136**, 1686–1699, https://doi.org/10.1002/qj.667.

Kieu, C., and Z. Moon, 2016: Hurricane intensity predictability. *Bull. Amer. Meteor. Soc.*, **97**, 1847–1857, https://doi.org/10.1175/BAMS-D-15-00168.1.

——, and Q. Wang, 2017: Stability of the tropical cyclone intensity equilibrium. *J. Atmos. Sci.*, **74**, 3591–3608, https://doi.org/10.1175/JAS-D-17-0028.1.

Knaff, J. A., C. Sampson, and M. DeMaria, 2005: An operational statistical typhoon intensity prediction scheme for the western North Pacific. *Wea. Forecasting*, **20**, 688–699, https://doi.org/10.1175/WAF863.1.

Kossin, J., 2018: A global slowdown of tropical-cyclone translation speed. *Nature*, **558**, 104–107, https://doi.org/10.1038/s41586-018-0158-3.

——, 2019: Reply to: Moon, I.-J. et al.; Lanzante, J. R. *Nature*, **570**, E16–E22, https://doi.org/10.1038/s41586-019-1224-1.

Li, L., and P. Chakraborty, 2020: Slower decay of landfalling hurricanes in a warming world. *Nature*, **587**, 230–234, https://doi.org/10.1038/s41586-020-2867-7.

Lilly, D. K., and K. Emanuel, 1985: A steady-state hurricane model. *16th Conf. on Hurricanes and Tropical Meteorology*, Houston, TX, Amer. Meteor. Soc., 142–143.

Liu, Y., D.-L. Zhang, and M. K. Yau, 2017: A multiscale numerical study of Hurricane Andrew (1992). Part I: Explicit simulation

and verification. *Mon. Wea. Rev.*, **125**, 3073–3093, https://doi.org/10.1175/1520-0493(1997)125<3073:AMNSOH>2.0.CO;2.

Marks, F. D., Jr., and Coauthors, 2008: Structure of the eye and eyewall of Hurricane Hugo (1989). *Mon. Wea. Rev.*, **136**, 1237–1259, https://doi.org/10.1175/2007MWR2073.1.

Molinari, J., and P. Duran, 2014: Low Richardson number in the tropical cyclone outflow layer. *J. Atmos. Sci.*, **71**, 3164–3179, https://doi.org/10.1175/JAS-D-14-0005.1.

Montgomery, M. T., J. Persing, and R. K. Smith, 2019: On the hypothesized outflow control of tropical cyclone intensification. *Quart. J. Roy. Meteor. Soc.*, **145**, 1309–1322, https://doi.org/10.1002/qj.3479.

Nolan, D., J. Zhang, and D. Stern, 2009: Evaluation of planetary boundary layer parameterizations in tropical cyclones by comparison of in-situ observations and high-resolution simulations of Hurricane Isabel (2003). Part I: Initialization, maximum winds, and the outer-core boundary layer. *Mon. Wea. Rev.*, **137**, 3651–3674, https://doi.org/10.1175/2009MWR2785.1.

Peng, K., R. Rotunno, and G. H. Bryan, 2018: Evaluation of a time-dependent model for the intensification of tropical cyclones. *J. Atmos. Sci.*, **75**, 2125–2138, https://doi.org/10.1175/JAS-D-17-0382.1.

——, ——, ——, and J. Fang, 2019: Evolution of an axisymmetric tropical cyclone before reaching slantwise moist neutrality. *J. Atmos. Sci.*, **76**, 1865–1884, https://doi.org/10.1175/JAS-D-18-0264.1.

Powell, M. D., P. J. Vickery, and T. A. Reinhold, 2003: Reduced drag coefficient for high wind speeds in tropical cyclones. *Nature*, **422**, 279–283, https://doi.org/10.1038/nature01481.

Ramsay, H., M. Singh, and D. R. Chavas, 2020: Response of tropical cyclone formation and intensification rates to climate warming in idealized simulations. *J. Adv. Model. Earth Syst.*, **12**, e2020MS002086, https://doi.org/10.1029/2020MS002086.

Rappaport, E., 2000: Loss of life in the United States associated with recent Atlantic tropical cyclones. *Bull. Amer. Meteor. Soc.*, **81**, 2065–2073, https://doi.org/10.1175/1520-0477(2000)081<2065:LOLITU>2.3.CO;2.

——, 2014: Fatalities in the United States from Atlantic tropical cyclones: New data and interpretation. *Bull. Amer. Meteor. Soc.*, **95**, 341–346, https://doi.org/10.1175/BAMS-D-12-00074.1.

Seidel, D. J., C. O. Ao, and K. Li, 2010: Estimating climatological planetary boundary layer heights from radiosonde observations: Comparison of methods and uncertainty analysis. *J. Geophys. Res.*, **115**, D16113, https://doi.org/10.1029/2009JD013680.

Shutts, G. J., 1981: Hurricane structure and the zero potential vorticity approximation. *Mon. Wea. Rev.*, **109**, 324–329, https://doi.org/10.1175/1520-0493(1981)109<0324:HSATZP>2.0.CO;2.

Smith, R. K., and M. T. Montgomery, 2010: Hurricane boundary-layer theory. *Quart. J. Roy. Meteor. Soc.*, **136**, 1665–1670, https://doi.org/10.1002/qj.679.

Stull, R. B., 1988: Boundary layer conditions and surface forcings. *An Introduction to Boundary Layer Meteorology*, R. B. Stull, Ed., Kluwer Academic Publishers, 261–270.

Tang, B., and K. Emanuel, 2010: Midlevel ventilation's constraint on tropical cyclone intensity. *J. Atmos. Sci.*, **67**, 1817–1830, https://doi.org/10.1175/2010JAS3318.1.

Tao, D., K. K. Emanuel, F. Zhang, R. Rotunno, M. M. Bell, and R. G. Nystrom, 2019: Evaluation of the assumptions in the steady-state tropical cyclone self-stratified outflow using three-dimensional convection-allowing simulations. *J. Atmos. Sci.*, **76**, 2995–3009, https://doi.org/10.1175/JAS-D-19-0033.1.

Tuleya, R. E., and Y. Kurihara, 1978: A numerical simulation of the landfall of tropical cyclones. *J. Atmos. Sci.*, **35**, 242–257, https://doi.org/10.1175/1520-0469(1978)035<0242:ANSOTL>2.0.CO;2.

Vickery, P. J., 2005: Simple empirical models for estimating the increase in the central pressure of tropical cyclones after landfall along the coastline of the United States. *J. Appl. Meteor.*, **44**, 1807–1826, https://doi.org/10.1175/JAM2310.1.

——, and L. Twisdale, 1995: Wind-field and filling models for hurricane wind-speed prediction. *J. Struct. Eng.*, **121**, 1700–1709, https://doi.org/10.1061/(ASCE)0733-9445(1995)121:11(1700).

——, P. F. Skerjl, and L. Twisdale, 2000: Simulation of hurricane risk in the U.S. using empirical track model. *J. Struct. Eng.*, **126**, 1222–1237, https://doi.org/10.1061/(ASCE)0733-9445(2000)126:10(1222).

Villarini, G., R. Goska, J. A. Smith, and G. A. Vecchi, 2014: North Atlantic tropical cyclones and U.S. flooding. *Bull. Amer. Meteor. Soc.*, **95**, 1381–1388, https://doi.org/10.1175/BAMS-D-13-00060.1.

Wong, M. L., J. C.-L. Chan, and W. Zhou, 2008: A simple empirical model for estimating the intensity change of tropical cyclones after landfall along the south China coast. *J. Appl. Meteor. Climatol.*, **47**, 326–338, https://doi.org/10.1175/2007JAMC1633.1.

Xi, D., N. N. Lin, and J. Smith, 2020: Evaluation of a physics-based tropical cyclone rainfall model for risk assessment. *J. Hydrometeor.*, **21**, 2197–2218, https://doi.org/10.1175/JHM-D-20-0035.1.

Zeng, J., and Q. Zhang, 2020: The trends in land surface heat fluxes over global monsoon domains and their responses to monsoon and precipitation. *Sci. Rep.*, **10**, 5762, https://doi.org/10.1038/s41598-020-62467-0.

Zhang, J. A., R. F. Rogers, D. S. Nolan, and F. D. Marks, 2011: On the characteristic height scales of the hurricane boundary layer. *Mon. Wea. Rev.*, **139**, 2523–2535, https://doi.org/10.1175/MWR-D-10-05017.1.